

Functionalized graphene origami metamaterials with tunable thermal conductivity



Jun Cai ^a, Ehsan Estakhrianhaghghi ^a, Abdolhamid Akbarzadeh ^{a,b,*}

^a Department of Bioresource Engineering, McGill University, Montreal, QC, H9X 3V9, Canada

^b Department of Mechanical Engineering, McGill University, Montreal, QC, H3A 0C3, Canada

ARTICLE INFO

Article history:

Received 5 October 2021

Received in revised form

1 February 2022

Accepted 3 February 2022

Available online 7 February 2022

Keywords:

Graphene

Origami

Tunable thermal conductivity

Surface functionalization

Nano-architected metamaterial

ABSTRACT

Graphene with tunable thermo-mechanical property is of great importance for next-generation thermal management devices. Distinct from previously reported porous graphene materials that tune the thermal conductivity at the cost of degrading their mechanical properties, non-porous hydrogenated graphene origami metamaterial exhibits a unique combination of tunable thermal conductivity, high strength, and enhanced stretchability. Through molecular dynamics simulation, a vast range of thermal conductivity can be found by tuning the geometrical parameters of the Miura-ori graphene origami, altering the adatom types and density, designing new origami patterns, and applying mechanical strains. By analyzing and comparing the numerical results from atomistic and continuum-based simulations, the effect of length scale on the thermal property of graphene origami metamaterials is explored. The temperature distribution, phonon density of states, phonon group velocity, and the atomic heat flux of the graphene origami are examined to illustrate the heat conduction mechanism. Finally, 3D graphene origami metamaterials are constructed by assembling the graphene origami strips, followed by evaluating their thermo-mechanical performance. Negative coefficients of thermal expansion are also observed in the functionalized graphene origami nanotubes. The introduced strategy for controlling the thermo-mechanical properties of graphene metamaterials can open up new avenues for developing thermoelectric devices, heat management systems, and flexible nanoelectronics.

© 2022 Elsevier Ltd. All rights reserved.

1. Introduction

Graphene, the classic one-atom thick two-dimensional (2D) material, has attracted intensive research interests owing to its outstanding thermo-electro-mechanical properties [1–5]. The monolayer graphene exhibits a unique combination of ultra-high mechanical property (Young's modulus of ~1 TPa and tensile strength of ~130 GPa [4]) and thermal conductivity (3000–5000 W m⁻¹ K⁻¹ for a suspended monolayer graphene [2,6]). The unique properties of graphene make it a promising candidate for flexible electronic devices [7,8], nanosensors [9], complementary metal-oxide-semiconductor [5], and nanoelectromechanical systems (NEMS) [10]. The multiphysical properties of graphene can be further tailored through defect engineering [9,11–14], mechanical strains [15,16], chemical functionalization [17,18], and doping

[11,19] to be adjusted for application requirements.

The requirements for multifunctional applications of graphene as thermoelectric and thermal management systems [15,16], electronic-skin [20], and flexible/wearable nanoelectronics [21–23] call for the tunability of their thermal properties (conductivity and expansion coefficient), enhanced stretchability, and high stiffness/strength. In principle, the thermal conductivity of graphene is dominated by the intrinsic phonon spectrum of carbon atoms, especially when the sample size is smaller than the average phonon mean free path (MFP) [24,25]. Based on recent experimental and numerical studies, one of the efficient strategies for tuning the thermal conductivity of graphene is defect engineering, such as applying specific cutting patterns (so-called "kirigami") [26,27], introducing voids and pores [14,28], or constructing 2D architected nanostructures [29]. The introduction of defects in graphene accelerates phonon scattering that softens phonon modes [15,16], resulting in the thermal conductivity reduction. Simultaneously, defect engineering affects the mechanical properties of graphene [13,21]. For example, a considerable enhancement in the stretchability of graphene has been observed in the experiment [26] and

* Corresponding author. Department of Bioresource Engineering, McGill University, Montreal, QC, H9X 3V9, Canada.

E-mail address: hamid.akbarzadeh@mcgill.ca (A. Akbarzadeh).

numerical simulations [21,23,27] through introducing kirigami patterns. For many applications in flexible and wearable nanoelectronics, graphene is required to demonstrate a high level of stretchability and ductile behavior [9]. However, this increase of stretchability is at the cost of the stiffness and strength reduction of graphene [12,16,21]. For instance, the strength of kirigami graphene with linear cuts is less than 15 GPa [21], around 10% of the pristine graphene. Another approach to minimize/tune the thermal conductivity of graphene is to synthesize graphene polymorphs and compounds [25] such as graphitic carbon-nitride ($\text{g-C}_3\text{N}_4$) [30], 36-6-Gdy [25], and boride-graphdiyne (C_{12}B_2) [25]. The strength of the graphene polymorphs and compounds is increased compared to the graphene kirigami; however, their stretchability is limited (~30%) [25]. For tuning the thermal expansion of graphene, approaches like introducing crystal defects [31] and doping [32] can be adopted; however, they result in a low strength (method of introducing crystal defects) or limited stretchability (doping). Trade-off between tunable thermal conductivity/expansion and mechanical (high strength/stretchability) properties of engineered graphene hampers reaching their full potential applications [9,16,21,23]. In efforts to combine tunable thermal properties with high strength and enhanced stretchability in graphene and nanomaterials, new design strategies should be developed.

Inspired by the old Chinese and Japanese art of paper folding [33,34], origami ('ori' means fold and 'kami' means paper) [26] approach might address the aforementioned thermo-mechanical property trade-off in graphene. Complex foldable graphene origami structures (GOSs) can be constructed out of a flexible one-atom-thick graphene sheet with creases introduced by surface functionalization, which forms a new sp^3 bond between the carbon atom and adatom [35–37]. The formation of atomic bonds in the graphene sheet is expected to decrease the thermal conductivity due to phonon scattering in the crease region formed by surface functionalization [38,39]. The origami approach can impart a design platform for developing nano/microstructured advanced materials with tunable coefficients of thermal expansion [40,41]. Simultaneously, the strength of GOS could be retained high since no cracks/voids are introduced during the graphene origami production.

This study explores the thermo-mechanical properties of GOS through molecular dynamics (MD) and finite element (FE) simulations. We first construct and consequently fold the graphene Miura-ori nanostructures via surface functionalization. The numerical results show that the thermal conductivity of GOS can be controlled by tuning the geometrical parameters and origami architectures, altering the adatom types and density, and applying mechanical strains. The tunability range of GOS thermal conductivity in this study can be from $0.2 \kappa_{e=0}$ to $4.8 \kappa_{e=0}$ by external mechanical strains ($\kappa_{e=0}$ is the thermal conductivity of GOS prior to mechanical deformation). The effect of length scale on GOS thermal conductivity is explored by scrutinizing the atomistic and continuum-based simulation results. The temperature distribution, phonon density of states, phonon group velocity, and the atomic heat flux of graphene origami are inspected to illustrate the heat conduction mechanism in these nano-architected metamaterials. Finally, 3D graphene origami nano-architected metamaterials are constructed based on the coupling and assembling of graphene origami strips and their thermo-mechanical performance is evaluated.

2. Methods

2.1. Molecular dynamics simulation

All atomic simulations are conducted using the large-scale

atomic molecular massively parallel simulator (LAMMPS) [42]. Open Visualization Tool (OVITO) [43] is employed to visualize the evolution of atomic structures. AIREBO [44] potential function is used to describe C–C and C–H interatomic interactions. The cutoff distance between C–C is set as 2.0 Å to avoid the spurious strengthening effect [28]. Periodic boundary conditions are applied to the planner directions, and a fixed boundary condition (the dimension of the box in the out-of-plane direction should be large enough to allow folding/unfolding of GOS) is used in the out-of-plane direction of GOS.

2.1.1. Constructing 3D graphene origami configuration

To transform a 2D flat graphene sheet to a 3D origami configuration, the surface functionalization is performed by placing hydrogen atoms, approximately in 1.1 Å distance from the adjacent carbon atom [35], in out-of-plane direction and on the top of the alternative carbon atoms (Figs. 1 and S1). When choosing nitrogen atom as an adatom to induce the folding of origami nanostructure, the distance between the carbon and nitrogen atoms is approximately 1.469 Å distance [45,46]. Initially, energy minimization is performed by a conjugate gradient algorithm. Then, the engineered hydrogenated graphene is relaxed at 300 K in the canonical ensemble (NVT) for 100 picoseconds (ps) and the isothermal-isobaric ensemble (NPT) for 3500 ps with a time step of 1.0 femtoseconds (fs). Then, a stable 3D graphene Miura-ori configuration can be obtained as shown in Figs. 1a to c.

2.1.2. Thermal conductivity calculation

Upon obtaining the stable graphene origami, the thermal conductivity of the GOS is studied by a reverse non-equilibrium MD (rNEMD) method, in which a heat flux is imposed on the GOS to generate a temperature gradient [16,44]. The system is divided into 50 slabs along the heat flow direction to extract the temperature profile. The heat and sink reservoirs are located in the middle and at the ends of the GOS, respectively. Since the configurations of GOS are different in x- and y-directions (Fig. 1b), we calculate and compare the thermal conductivities in these two directions by rNEMD method. To ensure that the calculated value represents the thermal conductivity of the GOS unit cell, computational models are constructed by duplicating the GOS unit cell along the direction of heat flux (such as the model shown in Fig. 1d for calculating the thermal conductivity in the y-direction) because the heat flux in rNEMD method travels through two opposite directions. After the full relaxation conducted in Section 2.1.1, the GOS is then switched to a micro-canonical ensemble (NVE) to conserve energy for 2×10^6 time steps (1 ns) with a time step of 0.5 fs. Finally, the kinetic energy is swapped between the coldest atoms in the heat sink slabs and the hottest atoms in the heat source in another NVE ensemble to induce the heat flux. The heat flux is then calculated by:

$$|\vec{J}| = \frac{\sum \frac{1}{2} (mv_h^2 - mv_c^2)}{At_{swap}} \quad (1)$$

where t_{swap} is the total time of exchanging kinetic energy, v_h and v_c are the velocities of atoms in the hot and cold slabs, and m is the atom mass, and A is the cross-sectional area of GOS. Here, we consider two different cross-sectional areas to calculate the GOS thermal conductivity in MD. The *atomic area* is the actual cross-sectional area for heat transfer (orange area in Fig. 1c), which can be used to explore the phonon scattering mechanism of GOS [47]. The *max area* represents the entire cross-sectional area of the unit cell (blue area in Fig. 1c). To compare our MD results with previously reported studies, we assume a thickness of 0.34 nm for all graphene sheets [16,28,48,49].

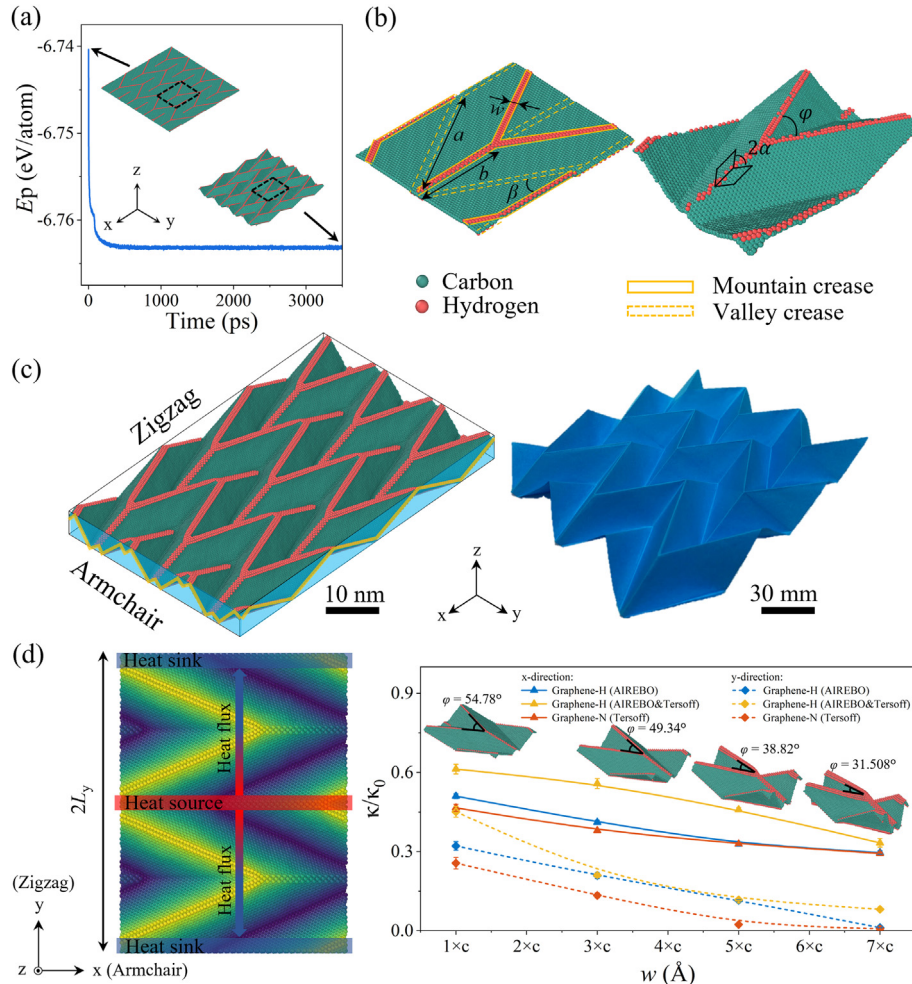


Fig. 1. Illustration of surface functionalization to transform a graphene sheet to a 3D origami nanostructure. (a) The potential energy of the GOS as a function of relaxation time in MD simulation (the unit cells are marked by the black dashed line). (b) Flat configuration of GOS (unit cell) with origami patterns and the folded configuration of GOS at an equilibrium state. (c) Graphene Miura-ori and paper Miura-ori origamis (3×3 unit cells). The orange area represents the atomic area, and the blue area represents the max area. (d) Model for rNEMD simulation of GOS and the normalized thermal conductivities of GOS in two orthogonal directions as a function of folding width w . The graphene-H and graphene-N represent the surface functionalized graphene by hydrogen and nitrogen atoms, respectively. The AIREBO and Tersoff represent the potential equation for the thermal conductivity calculation by MD simulation. For graphene-H (AIREBO), $\kappa_0 = 192.932$ W/mK and 163.663 W/mK in the x- (Armchair) and y-directions (Zigzag), respectively. For graphene-N (Tersoff) and graphene-H (AIREBO & Tersoff), $\kappa_0 = 236.29$ W/mK in the x-direction; $\kappa_0 = 212.779$ W/mK in the y-directions. (A colour version of this figure can be viewed online.)

Temperature distribution in the heat flux-direction is captured after 1 nanosecond (ns) when the system reaches the non-equilibrium steady state. The final temperature profiles are obtained by averaging the data of the last 4×10^6 time steps (2 ns). The temperature gradient ($\frac{\partial T}{\partial l}$) is obtained by a linear fitting in the labeled region (Fig. S5). Thermal conductivity is calculated by using the Fourier law as:

$$\kappa = \frac{|\vec{J}|}{\frac{\partial T}{\partial l}} \quad (2)$$

2.1.3. Thermal expansion calculation

To calculate the thermal expansion coefficient of GOS, after equilibrium at 300 K, the GOS is heated to 350 K (25 K/ns) and cooled to 250 K (−25 K/ns) using an NPT ensemble. The in-plane dimensions of GOS are recorded in the heating/cooling process. The thermal expansion of GOS is calculated by $\alpha = \frac{\Delta L}{L_0 \Delta T}$ where ΔL denotes the change in the length, L_0 is the initial length of GOS, and

ΔT represents the temperature change [40,41].

2.1.4. Mechanical deformation

To obtain the mechanical deformation of GOS, the sample is subjected to a homogeneous tensile/compressive deformation by rescaling the vertical coordinates of all atoms in the simulation box. In addition, the stress along the transverse direction is controlled by using NPT ensemble to ensure the uniaxial loading condition [21]. The strain rate is set at 1×10^9 s⁻¹. The axial tensile stress is calculated by averaging the virial stress of all atoms in the system.

2.2. Continuum approach

2.2.1. Detailed analysis

FE simulations are conducted using the commercially available ANSYS Workbench 2019 R2 software. The thermal transport within the graphene origami is simulated by employing steady-state thermal module. For thermal analysis, the temperature of one side is kept at 275 K while the temperature of the opposite side is set at 325 K. The remaining sides are thermally insulated (heat flux $J = 0$).

2.2.2. Computational standard mechanics homogenization

Under the assumption that the unit cell of GOS is repeated in x- and y-directions and the unit cell is far from the boundaries, we implement the homogenization technique to obtain effective properties of GOS when simulated as a continuum domain. The following boundary conditions and the independent unit thermal gradients are adopted on the boundaries in the x- and y-directions, a free boundary condition is applied in the z-direction [50]:

Periodicity in x-direction:

$$T(x_0, y) - T(x_0 + l_x, y) = l_x \left(\frac{\partial \bar{T}}{\partial x} \right)_i \quad (3)$$

Periodicity in y-direction:

$$T(x, y_0) - T(x, y_0 + l_y) = l_y \left(\frac{\partial \bar{T}}{\partial y} \right)_i \quad (4)$$

Independent unit thermal gradients:

$$(\bar{\nabla}T)_i = \left(\frac{\partial \bar{T}}{\partial x}, \frac{\partial \bar{T}}{\partial y} \right)_i = \begin{cases} (1, 0), & i = 1 \\ (0, 1), & i = 2 \end{cases} \quad (5)$$

where i is the thermal loading case number, x_0 and y_0 are the locations of the left and front faces of GOS unit cell, l_x and l_y are the dimensions of GOS unit cell along the x- and y-axes, and $\bar{\nabla}T$ is the average thermal gradient applied to the GOS unit cell.

The following linear relation between the heat flux (\vec{J}) and the temperature gradient ($\bar{\nabla}T$) is indicated by Fourier's law through a thermal conductivity tensor ($\bar{\kappa}$): $\vec{J} = -\bar{\kappa} \bar{\nabla}T$. For the origami structures in this research, we only care about the thermal conductivity in x- and y-directions. Hence, the thermal conductivity tensor is a symmetric 2×2 matrix κ , where $\kappa_{ij} = \kappa_{ji}$. The diagonal components (κ_{ii}) correlate the temperature gradient and heat flux along the primary direction of the coordinate system. Off-diagonal components (κ_{ij}) of the thermal conductivity tensor show the coupling effect between the temperature gradient in one direction and the heat flux normal to that direction. For thermally isotropic homogenous solid materials with thermal conductivity of κ , the thermal conductivity tensor is κI , where (I) is the identity tensor [50].

Based on the standard mechanical homogenization, the effective thermal conductivity of GOS can be determined by implementing periodic thermal conditions (Eqs. (3) and (4)) and separate unit thermal gradients (Eq. (5)) and measuring the volumetric average of the resulting heat flux as [50,51]:

$$\bar{\kappa}_{ij} = \frac{1}{V} \int \kappa_{ik} M_{kj}^T dV \quad (i, j, k = 1, 2) \quad (6)$$

where $\bar{\kappa}_{ij}$ is the effective thermal conductivity tensor, V represents the volume of the unit cell, κ_{ik} is the local thermal conductivity tensor, and M_{kj}^T matrix relates the average and the local temperature gradients by $\nabla T = M^T \bar{\nabla}T$.

3. Results and discussion

3.1. Functionalized graphene origami nanostructure and thermal transport

Fig. 1a and **b** show the surface functionalization of a graphene sheet by hydrogen atoms. The hydrogenation is applied to the carbon atoms within the area marked by yellow lines on the front side of the graphene sheet to generate mountain folds. On the

backside of the graphene sheet, the hydrogen atoms are placed on the top of carbon atoms within the area enclosed by the yellowish dash lines to generate valley folds (**Fig. 1b**). The potential energy (E_p) of GOS decreases monotonically to reach a minimum-energy equilibrium state after about 2000 ps (**Fig. 1a**), transforming a 2D graphene sheet into the well-known 3D Miura-ori origami nanostructure. Hydrogenation of a carbon atom in pristine graphene generates an sp^3-H bond (carbon-hydrogen bond, radial distribution function of GOS in **Fig. S3**). The hydrogen atom attracts the bonded carbon atoms, which induces accumulated distortion, transforming a 2D graphene sheet into a 3D graphene origami [37]. The generated graphene Miura-ori nanostructure, similar to its counterpart made by folding a paper at the macroscale (**Fig. 1c**), confirms the efficacy of surface functionalization for reconfiguration of graphene sheet into an origami nanostructure. More details of the surface functionalization and the evolution of GOS geometrical parameters during the relaxation process in MD simulation can be found in Supplementary Material S1 and S2.

We first perform MD simulations to study the effect of the folding width on the thermal conductivity of GOS. The proposed graphene Miura-ori configurations are characterized by $a = 123.04 \text{ \AA}$, $b = 83.17 \text{ \AA}$, and $\beta = 60^\circ$ (**Fig. 1d**). It is known that the degree of freedom of rigid origami is defined as $n - 3$ [33,52], where n is the number of edges at one vertex. The Miura-ori configuration with $n = 4$ has only one degree of freedom [52]. Hence, the angle between two adjacent parallelogram faces ($2\alpha \in [0, \pi]$ in **Fig. 1b**) can be applied to characterize the configuration of Miura-ori given a , b , and β (Supplementary Material S4). When the folding width (w , the width of hydrogenation strip) increases, the bending deformation accumulates accordingly, leading to the decrease of folding angle 2α . The folding angle 2α and folding width w show a linear relation independent of the lattice orientation (**Fig. S8**). However, this linear relation between 2α and w will be nonexistent when the folding width w reaches a critical value, where the corresponding folding angle $2\alpha = 0^\circ$. The critical folding width of GOS is about 9.0 \AA (**Fig. S8**). Here, four different folding widths ($w = 1 \times c \text{ \AA}$, $3 \times c \text{ \AA}$, $5 \times c \text{ \AA}$, and $7 \times c \text{ \AA}$, where $c = 1.23 \text{ \AA}$; the detailed definition of w can be found in Supplementary Material S5) are selected to investigate the effect of folding width on the thermal conductivity of GOS.

Fig. 1d depicts the computational modeling of GOS in MD simulation, where the heat source and sink slabs are located at the middle and the end of the system. **Fig. 1d** shows that the thermal conductivity of GOS decreases monotonically with the increased folding width in both x- (armchair) and y-directions (zigzag) based on atomic area. For hydrogenized graphene origami (graphene-H), the maximum reduction of thermal conductivity can be up to 93% when the folding width $w = 7 \times c \text{ \AA}$ in the y-direction. In addition, the reduction of thermal conductivity is more severe in the y-direction due to the different configurations of creases in the x- and y-directions. Since the graphene origami configurations are induced by surface functionalization via hydrogen atoms (graphene-H), which makes employing only Tersoff [53] potential function for calculating the GOS thermal properties impossible [28]. However, Tersoff potential is reported to better estimate the thermal conductivity of graphene due to its best performance of producing the phonon properties compared to AIREBO potential [53,54]. To exclude the possible reason that the tunable GOS thermal conductivity results from the selection of potential function, we calculate the GOS thermal conductivities based on two different potentials (**Fig. 1d**). First, we construct the GOss by applying nitrogen atoms (graphene-N) [55] and calculate the corresponding thermal conductivities characterized by different folding widths (w) based on Tersoff potential (**Fig. 1d**) [56]. Second, we combine Tersoff with AIREBO to calculate thermal conductivities of

graphene-H where Tersoff potential is applied to model the interactions between carbon atoms, and the cross-interactions between carbon and hydrogen atoms are modeled by AIREBO potential. We note that thermal conductivities of GOS based on different potentials (AIREBO, Tersoff) or different functionalization atoms (i.e., hydrogen and nitrogen) shows a similar trend with respect to the increasing folding width in both x- and y-directions, indicating that the reduction of thermal conductivity results from the origami configuration and the AIREBO potential can also be utilized to describe the thermal properties [15,16]. The difference between the thermal conductivities of graphene-H and graphene-N with the same folding width results from the different dimensions of origami configurations after relaxation (see Supplementary Material S6). Moreover, we aim to demonstrate that the origami engineering can be an effective strategy to tune the graphene thermal conductivity; the normalized effective thermal conductivity (κ/κ_0) is displayed in this research rather than its absolute magnitude. κ_0 in Fig. 1d is the thermal conductivity of pristine graphene with the same size as the flat configuration of GOS before relaxation (16.199 nm × 12.306 nm). The κ_0 for graphene-H (AIREBO) is calculated based on AIREBO [44] potential. The κ_0 for graphene-N (Tersoff) and graphene-H (AIREBO & Tersoff) are calculated based on Tersoff [53] potentials. The error bar shown in Fig. 1d is obtained from the linear fitting of the temperature gradient in MD simulation (Fig. S5). We also study the effect of chirality on the GOS thermal conductivity, which shows similar phenomena (see Supplementary Material S8). So far, the art of origami provides a potential thermal management solution.

3.2. Length-dependent thermal conductivity

The calculated thermal conductivity by rNEMD method is dependent on the size of the system due to finite sample size. The phonon scattering contributes to the thermal conductivity at the nanoscale, especially when the sample size is smaller than the average phonon MFP [24]. The length dependency of the thermal conductivity can be represented as: $\frac{1}{\kappa} = \frac{1}{\kappa_\infty} (1 + \frac{4}{L})$, where κ_∞ corresponds to the thermal conductivity of the sample with infinite length, λ donates an effective phonon MFP, and L represents the sample length along the thermal transport direction [25,57]. In Fig. 2a, we present the thermal conductivity of GOS versus the inverse of the sample length in the two main chirality-directions. To keep the same Miura-ori nanostructure, both sizes in the x- and y-directions are increased proportionally. The numerical results show an overall agreement with the length-dependent equation [25,57]; the thermal conductivity of GOS increases with the increased sample length. Following the relation: $\frac{1}{\kappa} = \frac{1}{\kappa_\infty} (1 + \frac{4}{L})$, the phonon MFP and κ_∞ of GOSs are obtained by fitting the MD data (Fig. 2a). As it can be seen, the phonon MFP does not show a significant change compared to the phonon MFP of graphene ($\lambda = 775$ nm) [58]. However, the κ_∞ obtained by fitting the MD results in Fig. 2a is affected by the graphene origami configuration, especially when $w = 7 \times c$. Since the thermal conductivity for pristine graphene at the microscale is around 3200 W/mK (Fig. 2b), the effects of the origami seem to work at the microscale from the fitting data. The reduction of thermal conductivity of graphene by introducing the origami creases at the nanoscale is due to the phonon scattering around the creases, while this mechanism disappears at the micro/mesoscale [21,23]. Hence, the effect of origami on the thermal conduction should not work at the microscale. We speculate that two factors lead to the decreased thermal conductivity of GOS at the microscale by fitting the MD results in Fig. 2a compared to the thermal conductivity of pristine graphene. First, the thermal conductivity with infinite length obtained by fitting the MD results

may include the effect of the phonon scattering. Second, the hydrogen atoms for surface functionalization decrease the thermal conductivity of GOS. To verify our speculation, we first calculate the thermal conductivity of graphene at the microscale and then calculate the thermal conductivity of GOS at the microscale by continuum approach.

Here, we only consider the thermal conductivity of GOS in the x-direction to study the scale effect. Before conducting the FE approach, the thermal conductivity of graphene at the microscale should be obtained firstly. Fig. 2b shows the thermal conductivity of the pristine graphene as a function of the length L ranging from 10 nm to 0.1 mm. The thermal conductivity of graphene at the nanoscale increases rapidly with the increased L because the phonon transport is ballistic. With the further increase of L , the thermal conductivity increases slowly due to the diffusive-ballistic transport of phonons. Finally, the thermal conductivity of graphene converges to a constant value, independent of the size at length L around ten microns, indicating the full diffusive transport of phonons. The size-dependent thermal conductivity of graphene from the ballistic regime to the diffusive regime can be described as [59]:

$$\kappa(L) = \frac{\kappa_\infty L^2}{2\pi^2 \lambda^2} \left(\sqrt{1 + 4 \left(\frac{\pi \lambda}{L} \right)^2} - 1 \right) \quad (7)$$

By fitting the MD results in Fig. 2b using Eq. (7), we determine the thermal conductivity of graphene with an infinite size $\kappa_0 = 3200$ W/mK and MFP $\lambda = 775$ nm. The calculated κ_0 of graphene with an infinite size falls within the range of experimental values 3000–5000 W/mK [58,60], and the MFP is the same as the previously reported data [58]. Then we input the obtained $\kappa_0 = 3200$ W/mK, the thermal conductivity of graphene at the microscale, into the FE approach to calculate the GOS thermal conductivity at the microscale. At the nanoscale, the folding width is comparable with the sample size, while at the micro/mesoscale, the folding width can be neglected (the FE origami model in Fig. 2c). The projection angle φ between two ridges is selected to represent the geometry of graphene Miura-ori samples (Fig. 2b and c). Details of the relationship between the geometry of Miura-ori and the geometrical parameters can be found in Supplementary Material S4. Fig. 2c and Table 1 report the tunable thermal conductivity of GOS in different length scales, in which the FE samples are characterized by $a = 12.304$ μm and $b = 8.317$ μm. Same as the MD simulation, two different cross-sectional areas are considered to calculate the GOS thermal conductivity in FE approach. From the calculation based on the atomic area, it is noted that, as expected, the thermal conductivity of GOS at the micro/mesoscale does not show a noticeable reduction compared to GOS at the nanoscale (Fig. 2c and Table 1). More specifically, the thermal conductivity of GOS at the microscale is around 90% of the pristine graphene. However, the highest thermal conductivity of GOS ($w = 1 \times c$ Å) at the nanoscale is about 51% of the pristine graphene, and the highest reduction of GOS ($w = 7 \times c$ Å) thermal conductivity compared with pristine graphene is nearly 69% at the nanoscale. Then, we plot the calculated thermal conductivity of GOS based on the atomic area with different lengths from 10 nm to 1 mm, which can be well fitted by Eq. (7) (Fig. 2d). Hence, the size-dependent thermal conductivities calculated based on the atomic area confirm that the thermal transport at the micro/mesoscale is dominated by the full diffusive transport of phonons and the reduction of thermal conductivity at the nanoscale is due to the phonon scattering around the origami creases. Next, we calculate the effective thermal conductivity of GOS based on the max area by MD and FM methods. Fig. 2c shows that the effective thermal conductivities based on max area are decreased compared to the results based on the atomic area due to

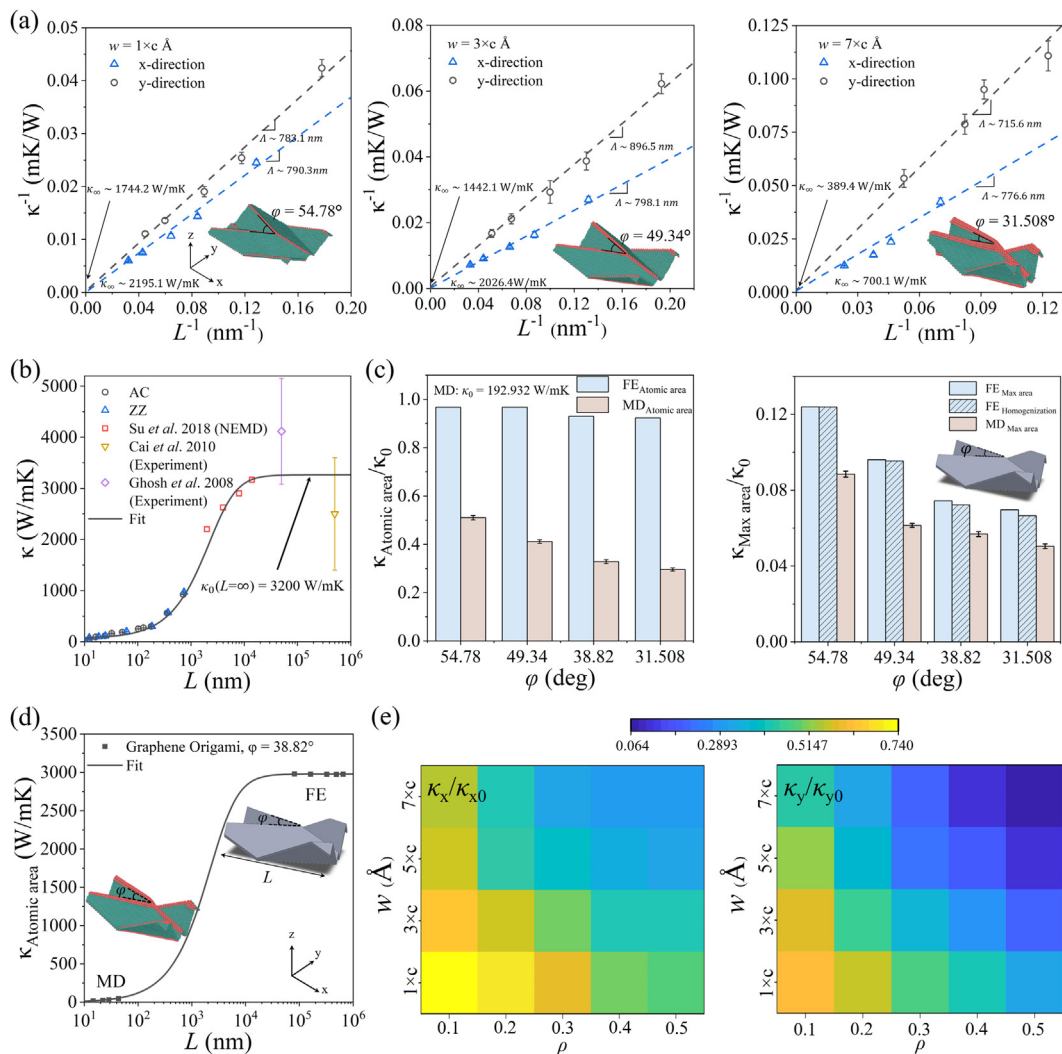


Fig. 2. (a) Thermal conductivity versus the inverse of the length for GOS. (b) The length dependence of thermal conductivity of pristine graphene. The data in Refs. [58,60,62] are indicated by the red rectangles, purple rhombus, and orange triangle, respectively. (c) The thermal conductivity of GOS calculated by MD and FE methods. κ_0 represents the thermal conductivity of pristine graphene. For MD simulation, $\kappa_0 = 192.932 \text{ W/mK}$ (at the nanoscale); For FE simulation, $\kappa_0 = 3200 \text{ W/mK}$ (at the microscale). (d) The length dependence of GOS thermal conductivity. (e) The effect of folding width on the thermal conductivity of GOS as a function of hydrogenation density. (A colour version of this figure can be viewed online.)

Table 1

Thermal conductivities of graphene origami characterized by different projection angles φ along the x-direction by different approaches. The size-dependent thermal conductivity of pristine graphene is κ_0 (MD) = 192.932 W/mK and κ_0 (FE) = 3200 W/mK .

| Approaches | $\varphi = 54.78^\circ$ | $\varphi = 49.34^\circ$ | $\varphi = 38.82^\circ$ | $\varphi = 31.508^\circ$ |
|-------------------|-------------------------|-------------------------|-------------------------|--------------------------|
| MD Atomic area | 98.40 | 79.31 | 63.36 | 60.41 |
| MD Max area | 17.07 | 11.85 | 10.96 | 9.74 |
| FE Atomic area | 3095.37 | 3004.33 | 2976.41 | 2954.15 |
| FE Max area | 396.45 | 307.49 | 238.20 | 222.84 |
| FE Homogenization | 396.34 | 305.13 | 231.15 | 212.83 |

the increased cross-sectional area for heat transfer in the calculation. The effective thermal conductivities calculated by MD and FE based on max area correspond to the thermal conductivity of the cuboid 3D structure (Fig. 1c), which are similar to the idea of a standard mechanics homogenization technique [50,51,61]. The homogenization technique is to find a homogenous medium equivalent to the original heterogeneous GOS. Thus, the results calculated by the FE with the max area and the homogenization

method are identical, as shown in Fig. 2c and Table 1. However, the effective thermal conductivities using MD based on the max area are smaller than the results obtained by FE and homogenization methods (Fig. 2c) due to different mechanisms. The phonons scattering around the creases and the increased cross-sectional area result in decreased effective thermal conductivities at the nanoscale. In contrast, the mechanism of phonons scattering does not work at the micro/mesoscale. Since we aim to investigate the tunable thermal conductivity of GOS and the mechanism of phonons transport behind the tunability in this research, we will calculate the thermal conductivity of GOS based on the atomic area in the following sections.

3.3. Effect of hydrogenation density

Next, we investigate the effect of hydrogenation density on the thermal conductivity of GOS. Figs. 1 and S7 show the complete hydrogenation pattern with the hydrogenation density, $\rho = 0.5$. The hydrogenation density is defined as the ratio between the number of hydrogen atoms and the number of carbon atoms within the

crease region (mountain crease and valley crease in Fig. 1b). Then, the hydrogen atoms are deleted randomly to construct the Miura-ori with the defective hydrogenation patterns. We note that the arrangement of hydrogen atoms has a limited effect on the Miura-ori configuration, and the bending deformation accumulates accordingly with the increased hydrogenation densities (Supplementary Material S10). Fig. 2e presents the calculated thermal conductivity of GOS as a function of hydrogenation density. For both cases of heat flux along the x- and y-directions, the thermal conductivity decreases with the increased hydrogenation density. Both the folding width and the hydrogenation density can tune the thermal conductivity of GOS effectively. Both heat flux directions show the same trend for thermal conductivity with respect to w and ρ in Fig. 2e. More specifically, increasing the folding width and the hydrogenation density result in decreased thermal conductivity. The tunability of GOS thermal conductivity in the y-direction shows a broader regulating range (from 0.064 κ_0 to 0.58 κ_0) compared to the x-direction. We also study the effect of temperature, graphene sheet layers, cell numbers, geometry, and the folding length ratio on the GOS thermal conductivity in Supplementary Material S11–S15.

3.4. Tunable thermal conductivity by mechanical strain

To explore the potential application of GOS as wearable and flexible electronic devices [7], we further study the mechanical properties and the strain effect on its thermal conductivity. Fig. 3a shows the typical stress-strain response and mechanical deformation of GOS characterized by $w = 7 \times c \text{ \AA}$ and $\rho = 0.4$ upon uniaxial compression/tension in the y-direction. Three distinct regimes can characterize the GOS stress-strain response: a plateau stress regime caused by the deformation of the creases (Regime II), the carbon atomic bonds stretching in tension (Regime III), and the densification of GOS in compression (Regime I). The GOS is finally broken along the creases (the region with hydrogen atoms) due to the stress concentration around creases (Fig. 3b). For comparison, a paper Miura-ori is fabricated by laser cutting machine (Trotec, Speedy 100) and folded by hands, as shown in Fig. 3c. The details of fabrication can be found in Supplementary Material S16. The paper Miura-ori shows a similar deformation process observed at the nanoscale by MD simulation (Fig. 3c and Video S1). The results obtained in the above sections suggest that the folded configurations of GOS are affected by the folding width w and hydrogenation density ρ , indicating that the mechanical response of GOS can also be dependent on w and ρ . The ultimate strength (peak stress, σ_u) and failure strain (ϵ_f) of GOS characterized by variable folding widths ($w = 1 \times c \text{ \AA}$, $3 \times c \text{ \AA}$, $5 \times c \text{ \AA}$, and $7 \times c \text{ \AA}$) and hydrogenation densities ($\rho = 0.1$, 0.2 , 0.3 , 0.4 , and 0.5) are shown in Fig. 3d. The strength, corresponding to failure stress, of GOS decreases with the increased folding width and hydrogenation density, whereas the failure strain shows the opposite trend. The folding of graphene sheets induced by the local bending is related to the hydrogenation of carbon atoms. The bending deformation accumulates accordingly with the increased folding width and hydrogenation density, which results in the high stretchability of GOS. The maximum failure strain of GOS ($w = 7 \times c \text{ \AA}$ and $\rho = 0.5$) is 1.015, five times over the pristine graphene ($\epsilon_f \approx 0.2$) [16]. In return, the hydrogenation of carbon atoms causes the stress concentration around the creases (Fig. 3b), leading to the strength decrease. However, the lowest strength of GOS ($w = 7 \times c \text{ \AA}$ and $\rho = 0.5$) is still about 28.2% of pristine graphene, and the highest strength ($w = 1 \times c \text{ \AA}$ and $\rho = 0.1$) is about 76.5% of pristine graphene. More details about the effect of hydrogenation density and folding width on mechanical properties can be found in Supplementary Material S17. We also report the results of Poisson's ratio of GOS in Fig. 3d. The creases

unfolding and folding processes in tension and compression lead to the lateral expansion/contraction, resulting in a negative Poisson's ratio [52]. The Poisson's ratio of graphene Miura-ori nanostructure can be calculated by:

$$\nu_{xy} = -\tan^2 \varphi / 2 \quad (8)$$

where φ is the projection angle between two ridges (details can be found in Supplementary Material S18). As shown in Fig. 3d, the Poisson's ratio of GOS obtained by MD simulation is consistent with the theoretical prediction. The Poisson's ratio of GOS increases with the increased folding width and hydrogenation density. Generally, the GOS mechanical response shows vast potential for flexible and wearable electronic nanodevices due to the low stiffness in the plateau-stress regime, stretchability/compressibility, and considerable high strength. Simultaneously, these mechanical properties can be tuned and programmed by altering the folding width and hydrogenation density.

Supplementary video related to this article can be found at <https://doi.org/10.1016/j.carbon.2022.02.008>.

After investigating the mechanical response of GOS, we turn our attention towards the effect of mechanical strain on the thermal conductivity of GOS. As shown in Fig. 3e, the thermal conductivity of GOS can be tuned by tension or compression. For the case of heat flux along (Fig. S25) or normal to (Fig. 3e) the tensile/compressive strain direction, the thermal conductivity increases with the increased tensile strains, contrary to the pristine graphene [63] and graphene kirigami [16]. In contrast, the thermal conductivity of GOS decreases by increased compressive strains. It is worth studying the tunability range of GOS thermal conductivity by applying a mechanical strain. The tunability range of thermal conductivity is defined as the differentials between the highest and lowest thermal conductivities of the GOS. For the heat flux normal to the mechanical strain (Fig. 3e), the highest tunability range of thermal conductivity is about 25% of κ_{x0} (κ_{x0} is the thermal conductivity of pristine graphene in the x-direction). For heat flux along with the mechanical strain (Fig. S25), the tunability range can be extended to 50% of κ_{y0} . The thermo-mechanical properties of GOS are studied by performing cyclic tensile/compressive tests at different levels of applied strains in Fig. S26. We find that the mechanical response of the GOS is largely reversible, and the GOS thermal conductivity is stable under the same mechanical strains at the different cyclic loading/unloading, suggesting potential utilization in wearable thermoelectric devices and flexible nanoelectronics.

3.5. New designs inspired by miura-ori patterns

Next, to further explore the tunability of GOS thermal conductivity, we construct different GOSs inspired by Miura-ori configurations (graphene origami C1–C7 in Supplementary Material S21). The new origami configurations are formed by rotating/shortening/curving certain creases in Miura-ori GOS. After arranging the hydrogen atoms in specific locations according to the designed origami patterns, the hydrogenized graphene sheets are relaxed in MD simulation to obtain a stable state with minimum potential energy and transform to 3D origami configurations. Then we apply the rNEMD method to calculate the thermal conductivity of newly designed GOS. Reported results in Fig. S29 illustrate that the thermal conductivity can be tailored by altering the origami patterns. Among all new designs, only the W-shape graphene Miura-ori (Fig. 4a) can be foldable, while the foldability of other GOS is extremely limited. Since we aim to explore the tunable thermal conductivity by external mechanical strains, only the design of C5

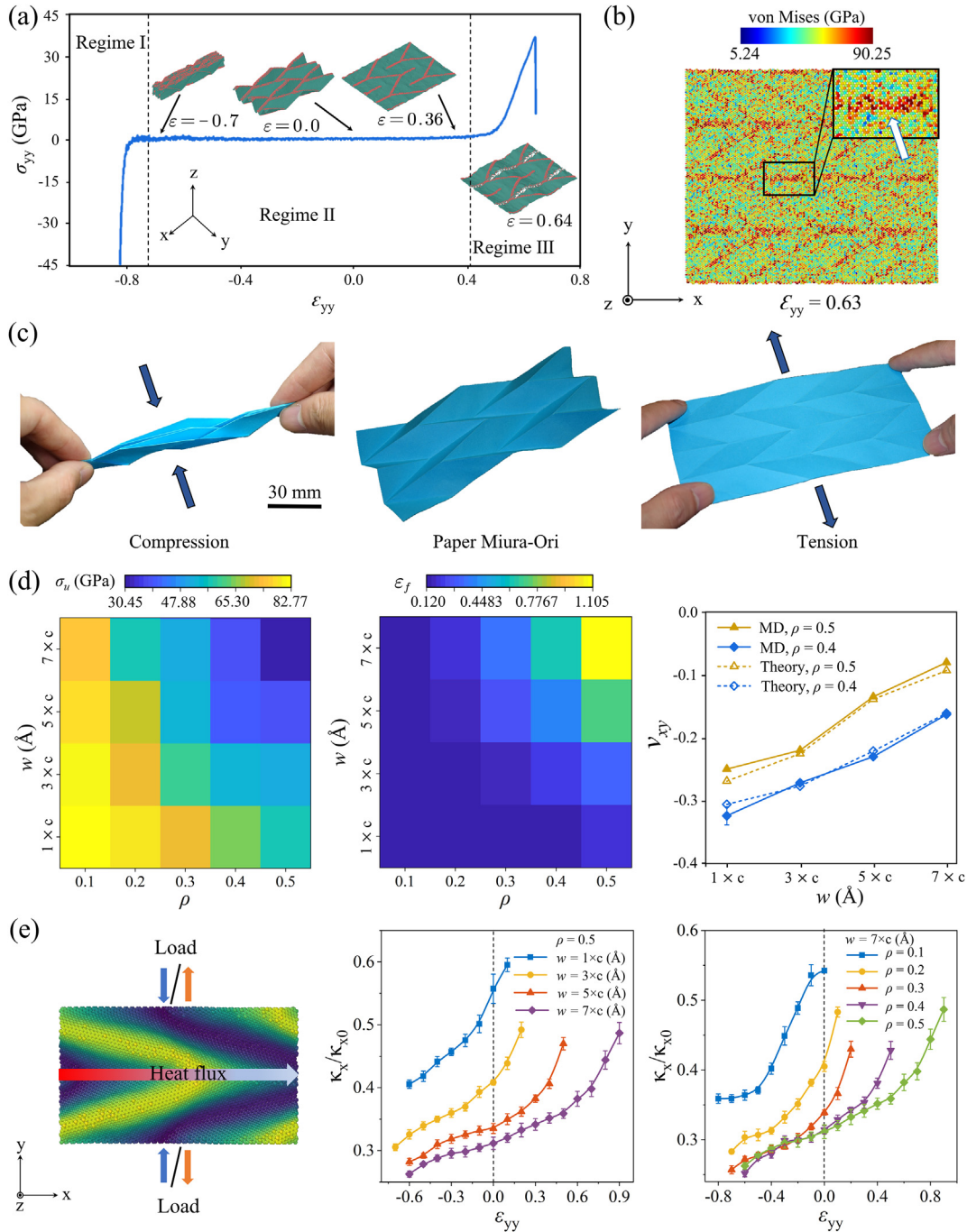


Fig. 3. (a) Stress-strain curve of GOS characterized by $w = 7 \times c \text{ \AA}$ and $\rho = 0.4$. (b) Von Mises stress distribution of GOS ($w = 7 \times c \text{ \AA}$ and $\rho = 0.4$) at strain $\epsilon = 0.63$. (c) Deformation of paper Miura-ori by hands. (d) The effect of folding width on strength and failure strain as a function of hydrogenation density. The Poisson's ratio ν_{xy} as a function of folding width. (e) Tunable thermal conductivity by mechanical strains. The heat flux-direction is normal to the loading direction. (A colour version of this figure can be viewed online.)

in Supplementary Material is discussed here. The W-shape graphene Miura-ori is constructed by replacing the crease a (white dashed line in Fig. 4a) with creases a_1 and a_2 with the included angles β_1 and β_2 . We consider two W-shape graphene Miura-ori models (W-1 and W-2) characterized by $\beta_1 = 30^\circ$ and $\beta_2 = 60^\circ$, $\beta_1 = \beta_2 = 30^\circ$, respectively (MD models in Fig. 4a and paper origami in Fig. 4b). It is found that the creases (a_1) with a longer length (smaller induced angle) can be fully folded, while the foldability of the creases (a_2) with a short length (large induced angle) is limited (Fig. 4c). The samples turn to be rigid after the crease a_1 is fully

folded. Since the length of crease a_1 in W-2 is longer than the crease a_1 in W-1, the W-2 sample shows a larger foldability range ($\epsilon_{yy} \approx -0.5$ to 0.247). As shown in Fig. 4c, the thermal conductivity of W-shape graphene Miura-ori can be effectively tuned by external mechanical strains. The tunability range of thermal conductivity is around 20% of κ_0 for all samples (κ_0 is the thermal conductivity of the pristine graphene with the same size as the flat configuration of W-shape GOS). Interestingly, due to the increased number of creases in W-shape graphene Miura-ori compared to the conventional graphene Miura-ori, the smallest thermal conductivity of W-

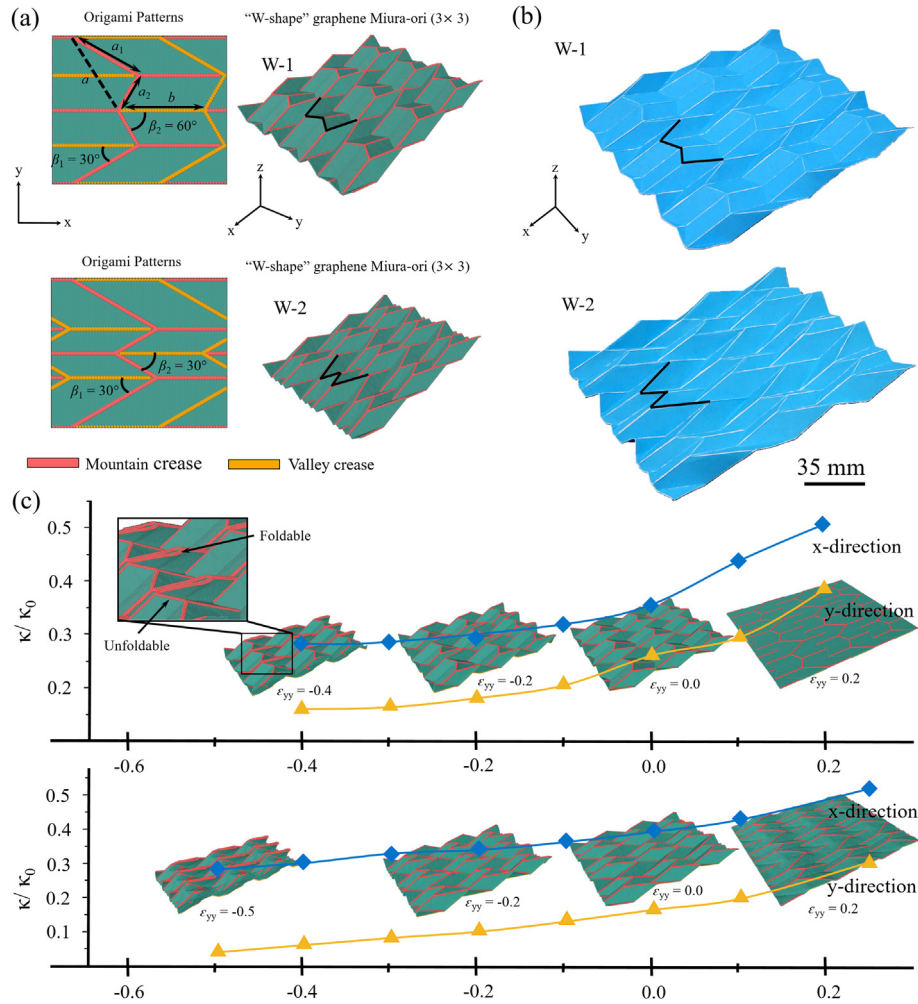


Fig. 4. W-shape graphene Miura-ori. (a) Nanoscale W-shape graphene Miura-ori (3×3 unit cells) in flat configurations with origami patterns and folded configurations (after relaxation). (b) The corresponding W-shape paper Miura-ori structures. (c) Tunable thermal conductivity of W-shape graphene Miura-ori via mechanical strains. (A colour version of this figure can be viewed online.)

2 is below 0.05 κ_0 when $\epsilon_{yy} = -0.5$ even the sample is not fully folded.

3.6. Mechanism governing the heat conduction

To better understand the mechanism governing the thermal conduction in GOS, we compare the temperature distribution of GOS ($\varphi = 38.82^\circ$) at the nano/microscales via MD and FE methods in Fig. 5a and b. For thermal transport at the nanoscale, temperature gaps can be observed clearly around the origami creases in both x- and y-directions, indicating that the creases hinder the temperature transport and induce a high interfacial thermal resistance (ITR). The temperature distribution of other Miura-ori inspired GOS reported in Supplementary Material S22 shows the same phenomenon as Fig. 5a and b. However, at the microscale, the temperature decreases uniformly/linearly along the thermal transport direction, and the creases seem not to act as a role of ITR.

Phonons, quanta of the crystal lattice vibrations, are usually the main heat carriers in carbon materials [64]. In 2D materials, such as graphene, acoustic phonons dominate the heat condition [65], which can be scattered by the other phonons, lattice defects, impurities, and interfaces [64–66]. The thermal conductivity of nanostructures is affected by the phonon energies, phonon group velocity, density of states (DOS), together with the phonon

scattering [65]. To explore the mechanism resulting in the reduction of thermal conductivity, the DOS of pristine graphene and GOS are firstly studied. The power spectrum is obtained by conducting fast Fourier transfer on the velocity autocorrelation function through a NVE run:

$$\text{DOS}_m(\omega) = \int_0^{\infty} \frac{\langle v_m(t)v_m(0) \rangle}{\langle v_m(0)v_m(0) \rangle} e^{-i\omega t} dt \quad (9)$$

where ω is the angular frequency and $v_m(t)$ represents the atomic velocity in the direction of $m = x, y$, and z at time t . We plot the DOS of pristine graphene and GOS characterized by different folding widths in Fig. 5c. The softening of phonon modes in high frequency (near 52 THz) is observed in x- and y-directions compared to pristine graphene. Moreover, a strong softening of phonon modes is observed in low frequency in the out-of-plane direction (z-direction) with the increased folding width, indicating the reduction of heat conduction. In addition, an inverse trend of phonon modes in high frequency in the out-of-plane direction is observed. However, the primary heat carrier of graphene is the acoustic phonons that belong to low frequency [25]. The phonon modes in high frequency are dominated by the in-plane directions. Hence, the strengthening of phonon modes in high frequency in the z-direction does not

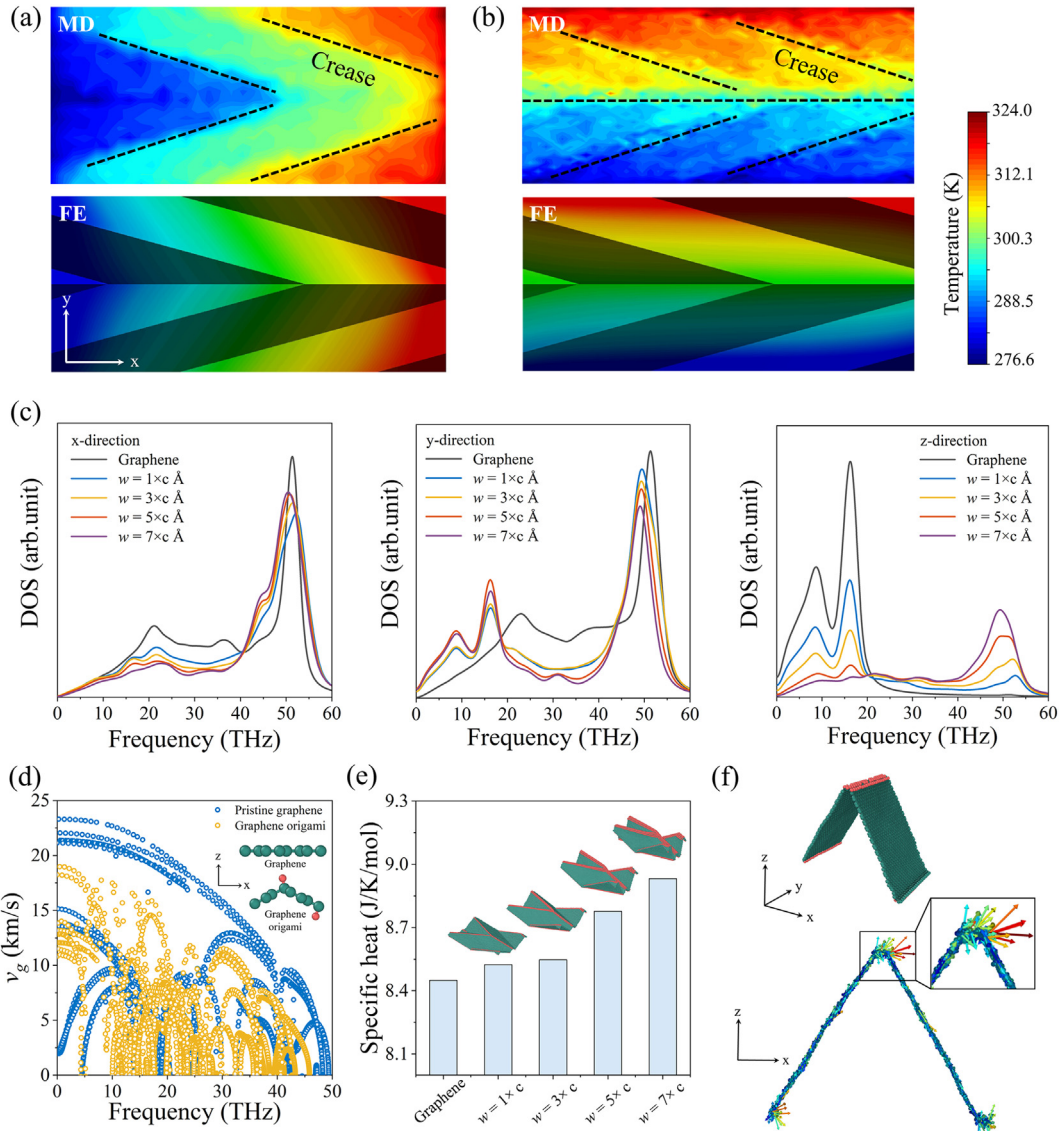


Fig. 5. Temperature distribution of GOS characterized by $w = 5 \times c \text{ \AA}$ and $\rho = 0.5$ for heat flow along (a) x- and (b) y-directions. (c) Phonon density of states of pristine graphene and GOS characterized by different folding widths. (d) Phonon group velocity (v_g) of pristine graphene and GOS. (e) Specific heat of pristine graphene and GOS characterized by different folding widths. (f) Spatial distribution of atomic heat flux by vector arrows in graphene origami. The color represents the magnitude of atomic heat flux in the x-direction. (A colour version of this figure can be viewed online.)

promote general thermal transport. It is known that phonon is a vibration of the atomic lattice; such vibrations pass through the whole lattice vibrating as a wave at a single frequency carrying heat [67]. The regularity of the lattice arrangement shows an important effect on the thermal conduction where the crystalline materials have a higher thermal conductivity than amorphous materials. Pristine graphene is a 2D crystal, even though it is not ideal because of the graphene atoms vibrating in three directions [65]. Hence, the observed softening of phonon modes of GOS compared to 2D crystal graphene may result from a reduction in the crystallinity of our system due to the self-folding of graphene induced by surface functionalization rather than the reduction of the phonon group velocity.

Further understanding of the mechanism governing the reduction of thermal reduction in GOS can be elucidated by studying the other influential factors, such as phonon group velocity and atomic heat flux. It is known that the thermal conductivity of nanomaterial is dominated by acoustic phonons, and is determined, among the

other factors, by the phonon group velocity of phonon modes [68,69]. The phonon group velocity of graphene and GOS are obtained by density-functional theory (DFT) based on first-principles calculations, which are performed by employing the open source code Quantum Espresso [70,71]. A graphene sheet with eight atoms and a simple graphene origami nanostructure with ten atoms are constructed with periodic boundary conditions in all directions. A vacuum space of at least 2 nm in the z-direction is inserted to eliminate the unnecessary interactions between adjacent systems due to the periodic boundary conditions. Fig. 5d shows an obvious depression of the phonon group velocity of GOS compared to pristine graphene, which results in the reduction of thermal conductivity since the phonons are usually the main heat carriers in carbon materials [64]. The specific heat (c_v) of pristine graphene and GOS characterized by different folding widths are presented in Fig. 5e, which represents the change in energy density U when the temperature changes by 1 K at a constant volume, $c_v = dU/dT \times 1/n$, where T is the absolute temperature and n denotes the

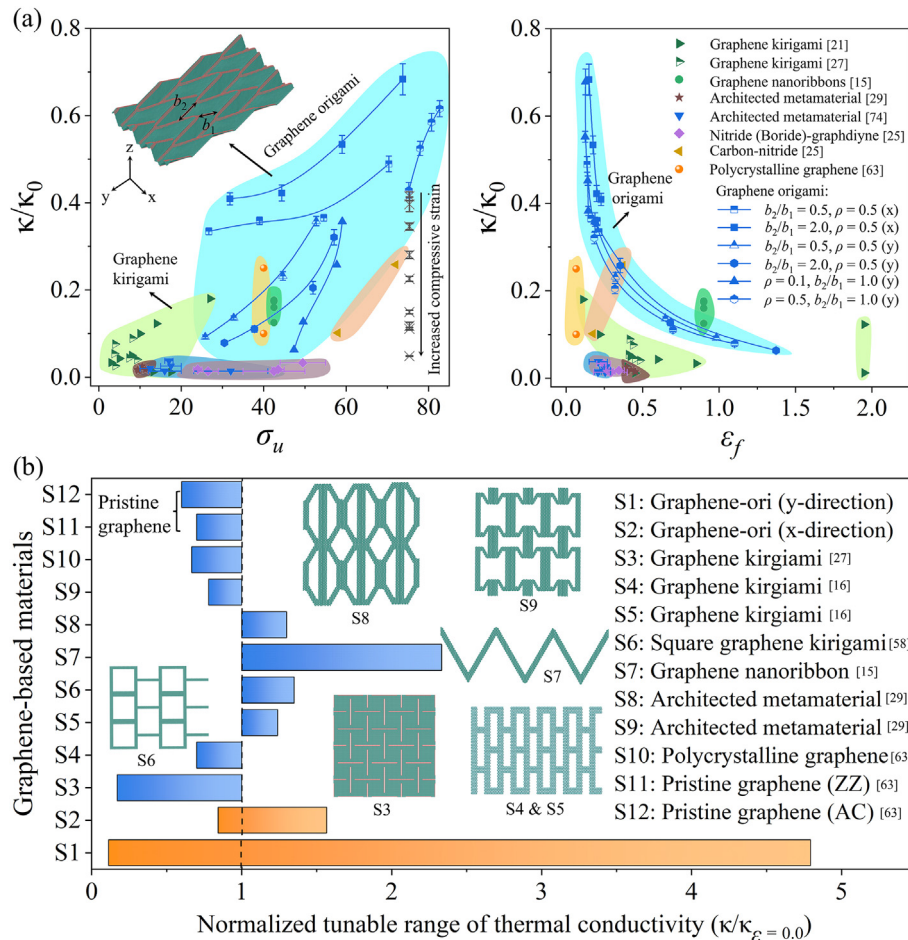


Fig. 6. Comparison of the thermo-mechanical performance of GOSs presented in this study and the other available graphene-based nanomaterials [15,21,25,27,29,63,74]. Thermal conductivity map plotted for graphene-based nanomaterials as a function of (a) strength (σ_u) and failure strain (ϵ_f). The “x” and “y” represent x- and y-direction, respectively. (b) Normalized thermal conductivity tunability range by applying mechanical strains (tension/compression) for graphene-architected metamaterials [15,16,27,29,63,74]. (A colour version of this figure can be viewed online.)

number of the atoms. The specific heat is not directly related to the thermal conductivity; however, it is an essential thermal property of nanomaterials and determines the thermal energy stored in the system and show how quickly the system cools down or heats up, referred as the thermal time constant τ ($\tau \approx RCV$, where R is the thermal resistance, C is specific heat, and V is the volume of the body) [72]. However, based on the Boltzmann transport equation (BTE) approach and single mode relaxation time (SMRT) approximation, a simple expression where the contribution to the thermal conductivity of each phonon mode i with momentum \mathbf{q} is $k_i(\mathbf{q}) = C_i(\mathbf{q})v_i^2(\mathbf{q})\tau_i^{ph}(\mathbf{q})$ [68,69], where $v_i(\mathbf{q})$ and $\tau_i^{ph}(\mathbf{q})$ are the group velocities and the lifetimes, respectively. $C_i(\mathbf{q})$ is the specific heat per unit volume of each vibrational state. Hence, for additional comparison, we calculate the specific heat of pristine graphene and GOS characterized by different folding widths in Fig. 5e. The specific heat of graphene is around 8.5 J/K/mol at 300 K, which is close to the reported results [72,73]. It is noted that the specific heat of GOS is higher than the graphene and increases with the increased folding widths. Lastly, we calculate the atomic heat flux, which is given by: $J_i = e_i v_i - S_i v_i$, where e_i , v_i , and S_i are the energy, velocity, and stress tensor of each atom i , respectively. The spatial distribution of the atomic heat flux by vector arrows in a simple graphene origami sample under non-equilibrium steady state is shown in Fig. 5f. A strong phonon scattering is observed at the crease region, which induces the reduction of thermal conductivity. On the other hand, the phonon scattering also confirms the temperature gaps

observed around origami creases in Fig. 5a and b.

3.7. Comparison of tunable thermal conductivity among alternative graphene-based nanomaterials

The abovementioned study concludes that the GOS shows excellent strength and stretchability. Herein, we plot a map for normalized thermal conductivity of GOS, graphene kirigami [16,21], graphene nanoribbons [15], graphene-architected metamaterials (S8 and S9 in Fig. 6) [29], nitride-graphdiyne [25], boride-graphdiyne [25], carbon-nitride [25], and polycrystalline graphene [63] as a function of ultimate strength (σ_u) and failure strain (ϵ_f) in Fig. 6a (κ_0 is the thermal conductivity of the pristine graphene with the same size as the corresponding graphene-based nanomaterials). The GOS presented in this work exhibits higher strength and failure strain than the majority of the other graphene-based nanomaterials. Some graphene kirigami nanostructures in Fig. 6a show greater stretchability than GOS, however, at the cost of very low strength ($\sigma_u \leq 5$ GPa). The GOS design broadens the material design space of nanomaterials, leading to the simultaneous tunability of thermal conductivity and high strength, while retaining a level of stretchability in the nanoarchitected metamaterial. Fig. 6a shows that the smallest thermal conductivity achieved by GOS is about $0.07\kappa_0$, which is a little higher than the other graphene nanoarchitected metamaterials. In addition to architectural design, mechanical strain is also an effective method

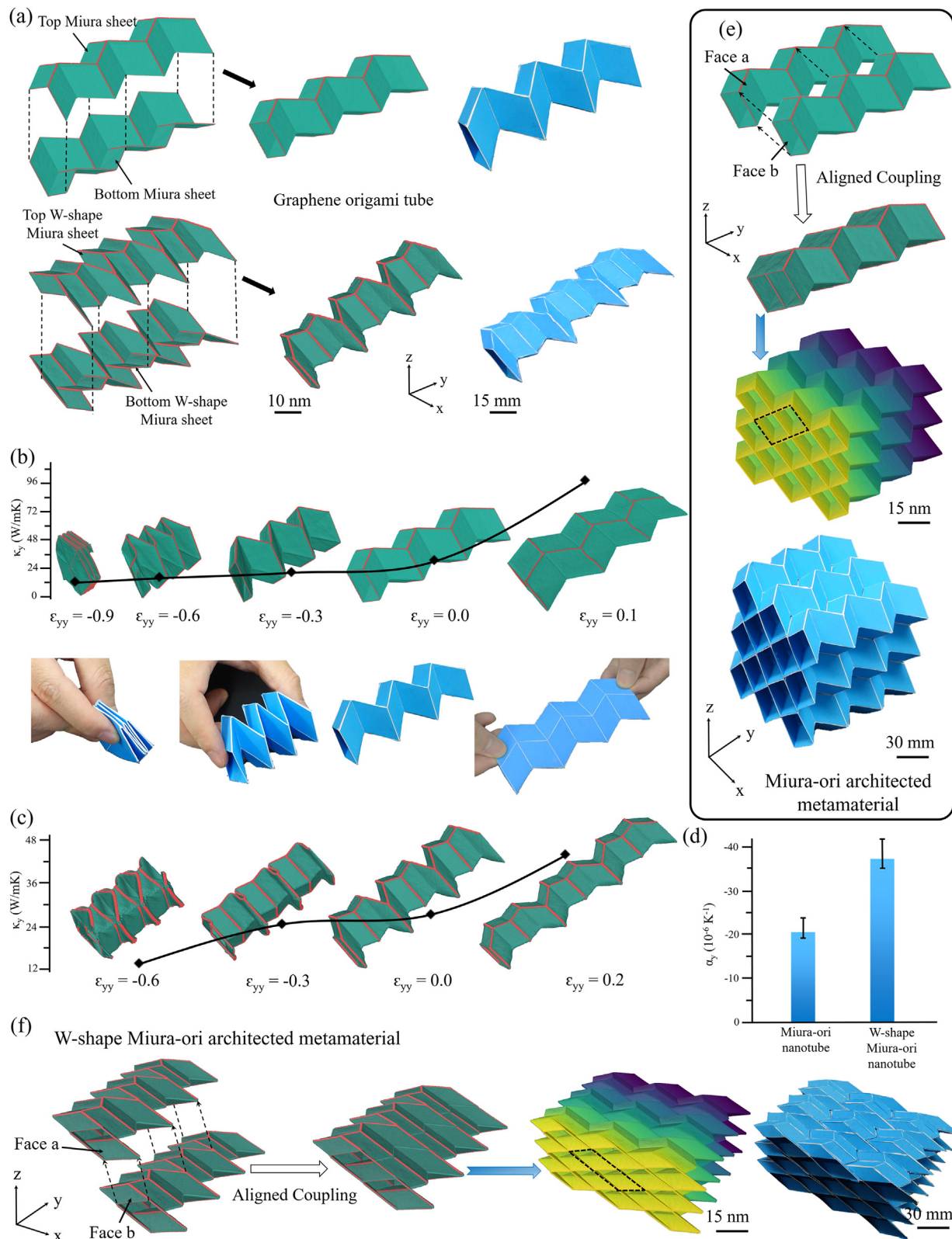


Fig. 7. 3D graphene origami architected metamaterial. (a) Miura-ori/W-shape strips and tube assembly. (b) Mechanical deformation process of graphene Miura-ori nanotube and the tunable thermal conductivity as a function of mechanical strains; Deformation of paper Miura-ori tube by hands. (c) Mechanical deformation process of graphene W-shape Miura-ori nanotube and the tunable thermal conductivity as a function of mechanical strains. (d) The thermal expansion coefficient of graphene origami nanotubes. (e) Schematic of combined 3D Miura-ori architected metamaterial. (f) Schematic of combined 3D W-shape Miura-ori architected metamaterial. (A colour version of this figure can be viewed online.)

for tuning the thermal conductivity of GOS (Fig. 3 and black markers in Fig. 6a). The thermal conductivity of the GOS ($w = 7 \times c$, $\rho = 0.5$, $b_2/b_1 = 1.0$) can be lower than $0.01\kappa_0$ when the compressive strain reaches 0.7. Another nanomaterial selection criterion is the tunability range of thermal conductivity by applying mechanical strains. In Fig. 6b, we compare the tunability range of GOS thermal conductivity in this work to other graphene-architected metamaterials [15,16,29,63,74] and pristine graphene [63] by applying mechanical strains, where the $\kappa_{e=0}$ is the thermal conductivity of the corresponding sample without mechanical deformation. The tunable range of GOS thermal conductivity in this work is from $0.2\kappa_{e=0}$ to $4.8\kappa_{e=0}$ in the y-direction and from $0.8\kappa_{e=0}$ to $1.1\kappa_{e=0}$ in the x-direction. The tunability range of GOS thermal conductivity in the y-direction is much larger than other graphene-architected metamaterials, indicating that the GOS in this study shows excellent thermal conductivity tunability by applying external mechanical strains. Moreover, the GOS can increase/decrease the thermal conductivity by applying the mechanical strains simultaneously, while other graphene-architected metamaterials can only realize one of the functionalities: reducing or increasing.

3.8. Enabling 3D graphene origami architected metamaterials

This section explores the possibility of building 3D graphene origami architected metamaterials at the nanoscale based on the coupling of GOSs. As shown in Fig. 7a, the graphene Miura-ori nanotube is assembled from two mirrored graphene Miura-ori strips characterized by $a = b$, $w = 3 \times c \text{ \AA}$, $\beta = 60^\circ$, and $\rho = 0.5$ (details about the assembly process of graphene Miura-ori tube in MD simulation can be found in Supplementary Material S24). The W-shape Miura-ori nanotube is constructed by coupling our newly designed graphene origami strips, as illustrated in Fig. 4a (W-1). The corresponding paper origami tubes are fabricated by laser cutting machine and glue, and then it is folded by hands. It is found that the Miura-ori nanotube can be fully folded in the y-direction (Fig. 7b, and Video S2), which shows a potential application in flexible thermoelectric nanodevices. However, the foldability of the W-shape Miura-ori nanotube is limited, in which only part of the creases can be fully folded (Fig. 7c, and Video S2). Instead, the stretchability of the W-shape Miura-ori nanotube is higher than Miura-ori nanotube due to the increased folding creases (Fig. S34). On the other hand, the thermal conductivities of these two nanotubes can be tuned effectively by mechanical strains. Even though the W-shape Miura-ori nanotube can not be fully folded, the thermal conductivity can be decreased as small as the Miura-ori nanotube resulting from the increased folding creases in the W-shape Miura-ori nanotube. We then calculate the thermal expansion coefficients of GOS and graphene origami nanotubes by MD simulation in Supplementary Material S25 and Fig. 7d. The previous researches [40,41] found that Miura-ori metamaterials provide a platform for designing systems with a broad range of thermal expansion coefficients at the nano-[40] and macroscales [41]. Results presented in Fig. S38 indicate that the thermal expansion coefficients (α_y) decrease with increased folding width (w) [40]. A very large negative thermal expansion coefficient in the y-direction ($\alpha_y = (-86.67 \pm 17.487) \times 10^{-6} \text{ K}^{-1}$) can be achieved when $w = 5 \times c$. In Fig. 7d, negative coefficients of thermal expansion are observed for graphene Miura-ori nanotube ($\alpha_y = (-20.63 \pm 1.425) \times 10^{-6} \text{ K}^{-1}$) and W-shape Miura-ori nanotube ($\alpha_y = (-37.195 \pm 2.337) \times 10^{-6} \text{ K}^{-1}$). Through the assembly of single graphene origami, multiple tubes are tessellated in the x- and y-directions to form a 3D graphene origami architected metamaterial, as shown in Fig. 7e and f (details about the 3D architected metamaterials can be found in Supplementary Material S26). It is worthwhile to mention that one of the faces ("face a" and "face b" in Fig. 7e and f) needs to be deleted for aligned coupling; the two tubes

are connected by the atomic bonds formed in the folding region (red lines). The 3D graphene origami architected metamaterials shown in Fig. 7e and f based on the coupling of Miura-ori tubes/W-shape Miura-ori tubes at the nanoscale can be of interest for further investigation and potential applications.

Supplementary video related to this article can be found at <https://doi.org/10.1016/j.carbon.2022.02.008>.

4. Concluding remarks

In summary, by employing the reverse non-equilibrium molecular dynamics method, we demonstrate that the hydrogenated graphene nanostructures provide a new platform for designing shape-changing graphene metamaterials with tunable thermal conductivity along with tailororable strength and failure strain, and thermal expansion coefficient. The graphene origami metamaterial is constructed via surface functionalization. The atomistic simulation results show that a vast range of thermal conductivity can be obtained by tuning the folding width and geometrical parameters, altering hydrogenation density and adatom types, and applying mechanical strains. Notably, the comparison between the atomistic and continuum-based simulation results shows that the effect of size-dependency on the thermal conductivity can be neglected when the size is far beyond the average phonon mean free path due to the transformation from ballistic to diffusive transport of phonons. The further results show that the softening of phonon modes, decreased phonon group velocity, and the phonon scattering around the creases decrease the thermal conductivity of graphene origami metamaterials. In addition, we construct the 3D graphene origami architected metamaterials at the nanoscale based on the coupling of functionalized graphene origami strips. The thermal conductivity of the assembled graphene origami nanotubes can be tuned by the external mechanical strains and the engineering origami patterns. Negative coefficients of thermal expansion are obtained in constructed graphene origami nanotubes. The functionalized origami nanostructure proposed here presents two main differences with respect to those reported graphene metamaterials: First, the proposed graphene metamaterials are intrinsically nonporous and therefore retain high strength; the stretchability is also increased compared to the pristine graphene. Second, the thermal conductivity can be increased by applying tension and decreased by applying compression, which displays a feasible strategy for adjusting the thermal conductivity of engineered nanomaterials. While here, we have focused on Miura-ori inspired origami configurations and the 3D graphene origami nanotubes by coupling the graphene origami strips at the nanoscale like the one shown in Fig. 7e, other topological reconfigurable origami architectures [34,75] or multistable shell-like lattices [76–78] can be also exploited at the nanoscale. Our study provides a new route for designing reconfigurable graphene metamaterials with tunable thermo-mechanical properties for potential applications in thermoelectric devices, nanoscale heat management systems, and flexible nanoelectronics.

CRediT authorship contribution statement

Jun Cai: Investigation, Validation, Methodology, Software, Data curation, Formal analysis, Writing – original draft, Writing – review & editing. **Ehsan Estakhrianaghghi:** Investigation, Writing – review & editing. **Abdolhamid Akbarzadeh:** Conceptualization, Investigation, Methodology, Supervision, Writing – review & editing, Funding acquisition.

Declaration of competing interest

The authors declare that they have no known competing

financial interests or personal relationships that could have appeared to influence the work reported in this paper.

Acknowledgement

This research was undertaken, in part, thanks to funding from the Canada Research Chairs program to A.H.Akbarzadeh in Multifunctional Metamaterials. A.H. Akbarzadeh also acknowledges the financial supports by Natural Sciences and Engineering Research Council of Canada through NSERC Discovery Grant (RGPIN-2016-0471) and Canada Foundation for Innovation (CFI) through John R. Evans Leaders Fund. J. Cai acknowledges the financial support provided by the China Scholarship Council [File No. 201909370077] and McGill University. This research was enabled by support provided by Calcul Quebec and Compute Canada. The authors acknowledge the contributions of Haoyu Chen and Youjian Li, in AM³L lab at McGill University, for the assists in the photography of prototyped samples.

Appendix A. Supplementary data

Supplementary data to this article can be found online at <https://doi.org/10.1016/j.carbon.2022.02.008>.

References

- [1] K.S. Novoselov, A.K. Geim, S.V. Morozov, D. Jiang, Y. Zhang, S.V. Dubonos, et al., Electric field effect in atomically thin carbon films, *Science* 306 (5696) (2004) 666–669.
- [2] S. Ghosh, W. Bao, D.L. Nika, S. Subrina, E.P. Pokatilov, C.N. Lau, et al., Dimensional crossover of thermal transport in few-layer graphene, *Nat. Mater.* 9 (7) (2010) 555–558.
- [3] W. Hu, Z. Li, J. Yang, Diamond as an inert substrate of graphene, *J. Chem. Phys.* 138 (5) (2013), 054701.
- [4] C. Lee, X. Wei, J.W. Kysar, J. Hone, Measurement of the elastic properties and intrinsic strength of monolayer graphene, *Science* 321 (5887) (2008) 385–388.
- [5] A.H. Castro Neto, The carbon new age, *Mater. Today* 13 (3) (2010) 12–17.
- [6] J.H. Seol, I. Jo, A.L. Moore, L. Lindsay, Z.H. Aitken, M.T. Pettes, et al., Two-dimensional phonon transport in supported graphene, *Science* 328 (5975) (2010) 213–216.
- [7] V. Strong, S. Dubin, M.F. El-Kady, A. Lech, Y. Wang, B.H. Weiller, et al., Patterning and electronic tuning of laser scribed graphene for flexible all-carbon devices, *ACS Nano* 6 (2) (2012) 1395–1403.
- [8] P. Avouris, Graphene: electronic and photonic properties and devices, *Nano Lett.* 10 (11) (2010) 4285–4294.
- [9] K. Yong, S. De, E.Y. Hsieh, J. Leem, N.R. Aluru, S. Nam, Kirigami-inspired strain-insensitive sensors based on atomically-thin materials, *Mater. Today* 34 (2019) 58–65.
- [10] C. Changyao, J. Hone, Graphene nanoelectromechanical systems, *Proc. IEEE* 101 (7) (2013) 1766–1779.
- [11] S. Hu, J. Chen, N. Yang, B. Li, Thermal transport in graphene with defect and doping: phonon modes analysis, *Carbon* 116 (2017) 139–144.
- [12] S. Dong, Y. Xia, R. Huang, J. Zhao, Modulating mechanical anisotropy of two-dimensional materials by controlling their defects, *Carbon* 158 (2020) 77–88.
- [13] B. Zheng, G.X. Gu, Tuning Graphene Mechanical Anisotropy via Defect Engineering, *Carbon*, 2019.
- [14] H. Wang, S. Hu, K. Takahashi, X. Zhang, H. Takamatsu, J. Chen, Experimental study of thermal rectification in suspended monolayer graphene, *Nat. Commun.* 8 (2017) 15843.
- [15] Y. Gao, W. Yang, B. Xu, Unusual thermal conductivity behavior of serpentine graphene nanoribbons under tensile strain, *Carbon* 96 (2016) 513–521.
- [16] N. Wei, Y. Chen, K. Cai, J. Zhao, H.-Q. Wang, J.-C. Zheng, Thermal conductivity of graphene kirigami: ultralow and strain robustness, *Carbon* 104 (2016) 203–213.
- [17] X. Mu, X. Wu, T. Zhang, D.B. Go, T. Luo, Thermal transport in graphene oxide—from ballistic extreme to amorphous limit, *Sci. Rep.* 4 (2014) 3909.
- [18] S.-K. Chien, Y.-T. Yang, Co-K Chen, Influence of chemisorption on the thermal conductivity of graphene nanoribbons, *Carbon* 50 (2) (2012) 421–428.
- [19] J.-W. Jiang, J. Lan, J.-S. Wang, B. Li, Isotopic effects on the thermal conductivity of graphene nanoribbons: localization mechanism, *J. Appl. Phys.* 107 (5) (2010).
- [20] P. Won, J.J. Park, T. Lee, I. Ha, S. Han, M. Choi, et al., Stretchable and transparent kirigami conductor of nanowire percolation network for electronic skin applications, *Nano Lett.* 19 (9) (2019) 6087–6096.
- [21] B. Mortazavi, A. Lherbier, Z. Fan, A. Harju, T. Rabczuk, J.C. Charlier, Thermal and electronic transport characteristics of highly stretchable graphene kirigami, *Nanoscale* 9 (42) (2017) 16329–16341.
- [22] L. Qiu, D. Li, H.M. Cheng, Structural control of graphene-based materials for unprecedented performance, *ACS Nano* 12 (6) (2018) 5085–5092.
- [23] Y. Gao, B. Xu, van der Waals graphene kirigami heterostructure for strain-controlled thermal transparency, *ACS Nano* 12 (11) (2018) 11254–11262.
- [24] X. Xu, L.F. Pereira, Y. Wang, J. Wu, K. Zhang, X. Zhao, et al., Length-dependent thermal conductivity in suspended single-layer graphene, *Nat. Commun.* 5 (2014) 3689.
- [25] S.M. Hatam-Lee, A. Rajabpour, S. Volz, Thermal conductivity of graphene polymorphs and compounds: from C3N to graphdiyne lattices, *Carbon* 161 (2020) 816–826.
- [26] M.K. Blees, A.W. Barnard, P.A. Rose, S.P. Roberts, K.L. McGill, P.Y. Huang, et al., Graphene kirigami, *Nature* 524 (7564) (2015) 204–207.
- [27] J. Cai, A. Akbarzadeh, Hierarchical Kirigami-Inspired Graphene and Carbon Nanotube Metamaterials: Tunability of Thermo-Mechanic Properties, *Materials & Design*, 2021, p. 206.
- [28] H. Ghasemi, A. Rajabpour, A.H. Akbarzadeh, Tuning thermal conductivity of porous graphene by pore topology engineering: comparison of non-equilibrium molecular dynamics and finite element study, *Int. J. Heat Mass Tran.* 123 (2018) 261–271.
- [29] Y. Gao, W. Yang, B. Xu, Tailoring auxetic and contractile graphene to achieve interface structures with fully mechanically controllable thermal transports, *Adv. Mater. Interfac.* 4 (11) (2017).
- [30] G. Algara-Siller, N. Severin, S.Y. Chong, T. Bjorkman, R.G. Palgrave, A. Laybourn, et al., Triazine-based graphitic carbon nitride: a two-dimensional semiconductor, *Angew. Chem. Int. Ed. Engl.* 53 (29) (2014) 7450–7455.
- [31] G. López-Polín, M. Ortega, J.G. Vilhena, I. Alda, J. Gomez-Herrero, P.A. Serena, et al., Tailoring the thermal expansion of graphene via controlled defect creation, *Carbon* 116 (2017) 670–677.
- [32] S. Mann, R. Kumar, V.K. Jindal, Negative thermal expansion of pure and doped graphene, *RSC Adv.* 7 (36) (2017) 22378–22387.
- [33] L. Yuan, H. Dai, J. Song, J. Ma, Y. Chen, The Behavior of a Functionally Graded Origami Structure Subjected to Quasi-Static Compression, *Materials & Design*, 2020, p. 189.
- [34] Z. Lin, L.S. Novelino, H. Wei, N.A. Alderete, G.H. Paulino, H.D. Espinosa, et al., Folding at the microscale: enabling multifunctional 3D origami-architected metamaterials, *Small* (2020), e2002229.
- [35] C.D. Reddy, Y.W. Zhang, Structure manipulation of graphene by hydrogenation, *Carbon* 69 (2014) 86–91.
- [36] N. Wei, Y. Chen, Y. Zhang, J.-C. Zheng, J. Zhao, Y.-W. Mai, Crease-induced targeted cutting and folding of graphene origami, *Carbon* 165 (2020) 259–266.
- [37] S. Zhu, T. Li, Hydrogenation-assisted graphene origami and its application in programmable molecular mass uptake, storage, and release, *ACS Nano* 8 (3) (2014) 2864–2872.
- [38] B. Mortazavi, E.V. Podryabinkin, S. Roche, T. Rabczuk, X. Zhuang, A.V. Shapeev, Machine-learning interatomic potentials enable first-principles multiscale modeling of lattice thermal conductivity in graphene/borophene heterostructures, *Mater. Horiz.* 7 (9) (2020) 2359–2367.
- [39] W. Ning, Y. Chen, K. Cai, Y. Zhang, Q. Pei, J.-C. Zheng, et al., Unusual Thermal Properties of Graphene Origami Crease: A Molecular Dynamics Study, *Green Energy & Environment*, 2020.
- [40] D.T. Ho, H.S. Park, S.Y. Kim, U. Schwingenschlogl, Graphene origami with highly tunable coefficient of thermal expansion, *ACS Nano* 14 (7) (2020) 8969–8974.
- [41] E. Boatti, N. Vasilios, K. Bertoldi, Origami metamaterials for tunable thermal expansion, *Adv. Mater.* 29 (26) (2017).
- [42] S. Plimpton, Fast parallel algorithms for short-range molecular dynamics, *J. Comput. Phys.* 117 (1) (1995) 1–19.
- [43] A. Stukowski, Visualization and analysis of atomistic simulation data with OVITO—the Open Visualization Tool, *Model. Simulat. Mater. Sci. Eng.* 18 (1) (2010).
- [44] F. Müller-Plathe, A simple nonequilibrium molecular dynamics method for calculating the thermal conductivity, *J. Chem. Phys.* 106 (14) (1997) 6082–6085.
- [45] J.P. Paolini, The bond order?bond length relationship, *J. Comput. Chem.* 11 (10) (1990) 1160–1163.
- [46] K. Jug, D.N. Nanda, SINDO1 II. Application to ground states of molecules containing carbon, nitrogen and oxygen atoms, *Theor. Chim. Acta* 57 (2) (1980) 107–130.
- [47] C. Zhang, A. Akbarzadeh, W. Kang, J. Wang, A. Mirabolghasemi, Nano-architected metamaterials: carbon nanotube-based nanotrusses, *Carbon* 131 (2018) 38–46.
- [48] R. Grantab, V.B. Shenoy, R.S. Ruoff, Anomalous strength characteristics of tilt grain boundaries in graphene, *Science* 330 (6006) (2010) 946–948.
- [49] S. Stankovich, D.A. Dikin, R.D. Piner, K.A. Kohlhaas, A. Kleinhammes, Y. Jia, et al., Synthesis of graphene-based nanosheets via chemical reduction of exfoliated graphite oxide, *Carbon* 45 (7) (2007) 1558–1565.
- [50] A. Mirabolghasemi, A.H. Akbarzadeh, D. Rodrigue, D. Therriault, Thermal conductivity of architected cellular metamaterials, *Acta Mater.* 174 (2019) 61–80.
- [51] A.H. Akbarzadeh, J.W. Fu, L. Liu, Z.T. Chen, D. Pasini, Electrically conducting sandwich cylinder with a planar lattice core under prescribed eigenstrain and magnetic field, *Compos. Struct.* 153 (2016) 632–644.
- [52] C. Lv, D. Krishnaraju, G. Konjevod, H. Yu, H. Jiang, Origami based mechanical metamaterials, *Sci. Rep.* 4 (2014) 5979.

- [53] L. Lindsay, D.A. Broido, Optimized Tersoff and Brenner empirical potential parameters for lattice dynamics and phonon thermal transport in carbon nanotubes and graphene, *Phys. Rev. B* 81 (20) (2010).
- [54] E.N. Koukaras, G. Kalosakas, C. Galiotis, K. Papagelis, Phonon properties of graphene derived from molecular dynamics simulations, *Sci. Rep.* 5 (2015) 12923.
- [55] D.T. Ho, V.H. Ho, V. Babar, S.Y. Kim, U. Schwingenschlogl, Complex three-dimensional graphene structures driven by surface functionalization, *Nanoscale* 12 (18) (2020) 10172–10179.
- [56] A. Kinaci, J.B. Haskins, C. Sevik, T. Çağın, Thermal conductivity of BN-C nanostructures, *Phys. Rev. B* 86 (11) (2012).
- [57] X. Zhang, H. Xie, M. Hu, H. Bao, S. Yue, G. Qin, et al., Thermal conductivity of silicene calculated using an optimized Stillinger-Weber potential, *Phys. Rev. B* 89 (5) (2014).
- [58] S. Ghosh, I. Calizo, D. Teweldebrhan, E.P. Pokatilov, D.L. Nika, A.A. Balandin, et al., Extremely high thermal conductivity of graphene: prospects for thermal management applications in nanoelectronic circuits, *Appl. Phys. Lett.* 92 (15) (2008).
- [59] F.X. Alvarez, D. Jou, Memory and nonlocal effects in heat transport: from diffusive to ballistic regimes, *Appl. Phys. Lett.* 90 (8) (2007).
- [60] W. Cai, A.L. Moore, Y. Zhu, X. Li, S. Chen, L. Shi, et al., Thermal transport in suspended and supported monolayer graphene grown by chemical vapor deposition, *Nano Lett.* 10 (5) (2010) 1645–1651.
- [61] J. Shi, A.H. Akbarzadeh, Architected cellular piezoelectric metamaterials: thermo-electro-mechanical properties, *Acta Mater.* 163 (2019) 91–121.
- [62] R. Su, X. Zhang, Size effect of thermal conductivity in monolayer graphene, *Appl. Therm. Eng.* 144 (2018) 488–494.
- [63] S. Bazrafshan, A. Rajabpour, Engineering of thermal transport in graphene using grain size, strain, nitrogen and boron doping; a multiscale modeling, *Int. J. Heat Mass Tran.* 123 (2018) 534–543.
- [64] J.M. Ziman, *Electrons and Phonons: the Theory of Transport Phenomena in Solids*, Oxford university press, 2001.
- [65] D.L. Nika, A.A. Balandin, Two-dimensional phonon transport in graphene, *J. Phys. Condens. Matter* 24 (23) (2012) 233203.
- [66] J. Callaway, Model for lattice thermal conductivity at low temperatures, *Phys. Rev.* 113 (4) (1959) 1046–1051.
- [67] S.H. Simon, *The Oxford Solid State Basics*, OUP, Oxford, 2013.
- [68] D. Donadio, G. Galli, Thermal conductivity of isolated and interacting carbon nanotubes: comparing results from molecular dynamics and the Boltzmann transport equation, *Phys. Rev. Lett.* 99 (25) (2007) 255502.
- [69] W.A. Diery, E.A. Moujaes, R.W. Nunes, Nature of localized phonon modes of tilt grain boundaries in graphene, *Carbon* 140 (2018) 250–258.
- [70] P. Giannozzi, O. Andreussi, T. Brumme, O. Bunau, M. Buongiorno Nardelli, M. Calandra, et al., Advanced capabilities for materials modelling with Quantum ESPRESSO, *J. Phys. Condens. Matter* 29 (46) (2017) 465901.
- [71] P. Giannozzi, S. Baroni, N. Bonini, M. Calandra, R. Car, C. Cavazzoni, et al., Quantum espresso: a modular and open-source software project for quantum simulations of materials, *J. Phys. Condens. Matter* 21 (39) (2009) 395502.
- [72] E. Pop, V. Varshney, A.K. Roy, Thermal properties of graphene: fundamentals and applications, *MRS Bull.* 37 (12) (2012) 1273–1281.
- [73] N. Mounet, N. Marzari, First-principles determination of the structural, vibrational and thermodynamic properties of diamond, graphite, and derivatives, *Phys. Rev. B* 71 (20) (2005).
- [74] H. Li, G. Cheng, Y. Liu, D. Zhong, Anomalous thermal response of graphene kirigami induced by tailored shape to uniaxial tensile strain: a molecular dynamics study, *Nanomaterials* 10 (1) (2020).
- [75] M. Eidini, G.H. Paulino, Unraveling metamaterial properties in zigzag-base folded sheets, *Sci. Adv.* 1 (8) (2015), e1500224.
- [76] J. Shi, H. Mofatteh, A. Mirabolghasemi, G. Desharnais, A. Akbarzadeh, Programmable multistable perforated shellular, *Adv. Mater.* (2021), e2102423.
- [77] S.J.P. Callens, N. Tümer, A.A. Zadpoor, Hyperbolic origami-inspired folding of triply periodic minimal surface structures, *Appl. Mater. Today* 15 (2019) 453–461.
- [78] M. Akbari, A. Mirabolghasemi, M. Bolhassani, A. Akbarzadeh, M. Akbarzadeh, Strut-based cellular to shellular funicular materials, *Adv. Funct. Mater.* (2022), e2109725.